

Swift panchromatic observations of the bright gamma-ray burst GRB050525a

A. J. Blustin¹, D. Band², S. Barthelmy², P. Boyd², M. Capalbi⁴, S. T. Holland², F. E. Marshall², K. O. Mason¹, M. Perri⁴, T. Poole¹, P. Roming³, S. Rosen¹, P. Schady^{1,3}, M. Still², B. Zhang⁵, L. Angelini², L. Barbier², A. Beardmore⁶, A. Breeveld¹, D. N. Burrows³, J. R. Cummings², J. Canizzo², S. Campana⁸, M. M. Chester³, G. Chincarini⁸, L.R. Cominsky⁹, A. Cucchiara³, M. de Pasquale¹, E.E. Fenimore⁷, N. Gehrels², P. Giommi⁴, M. Goad⁶, C. Gronwall³, D. Grupe³, J.E. Hill², D. Hinshaw², S. Hunsberger³, K.C. Hurley¹¹, M. Ivanushkina³, J.A. Kennea³, H. A. Krimm², P. Kumar, W. Landsman², V. La Parola¹⁰, C. B. Markwardt², K. McGowan¹, P. Mészáros³, T. Mineo¹⁰, A. Moretti⁸, A. Morgan³, J. Nousek³, P.T. O'Brien⁶, J.P. Osborne⁶, K. Page⁶, M. J. Page¹, D. M. Palmer⁷, A.M. Parsons², J. Rhoads¹³, P. Romano⁸, T. Sakamoto², G. Sato¹², G. Tagliaferri⁸, J. Tueller², A.A. Wells⁶ & N. E. White²

¹ *Mullard Space Science Laboratory, Department of Space and Climate Physics, University College London, Holmbury St Mary, Dorking, Surrey, RH5 6NT, UK.*

² *NASA/Goddard Space Flight Center, Greenbelt, MD 20771, USA.*

³ *Department of Astronomy and Astrophysics, Pennsylvania State University, 525 Davey Laboratory, University Park, PA 16802, USA.*

⁴ *ASI Science Data Center, Via Galileo Galilei, I-00044 Frascati, Italy.*

⁵ *Department of Physics, University of Nevada, Las Vegas, NV 89154, USA.*

⁶ *Department of Physics & Astronomy, University of Leicester, Leicester LE1 7RH, UK.*

⁷ *Los Alamos National Laboratory, Los Alamos, New Mexico 87545, USA.*

⁸ *INAF - Osservatorio Astronomico di Brera, Via Bianchi 46, I-23807 Merate, Italy.*

¹⁰ *INAF - Istituto di Astrofisica Spaziale e Cosmica, Via Ugo La Malfa 153, I-90146 Palermo, Italy.*

¹¹ *UC Berkeley Space Sciences Laboratory, Berkeley, CA 94720, USA.*

¹² *Institute of Space and Astronautical Science, Kanagawa 229-8510, Japan.*

¹³ *Space Telescope Science Institute, 3700 San Martin Drive, Baltimore, MD 21218, USA.*

ajb@mssl.ucl.ac.uk

ABSTRACT

The bright gamma-ray burst GRB050525a has been detected with the Swift observatory, providing unique multiwavelength coverage from the very earliest phases of the burst. The X-ray and optical/UV afterglow decay light curves

both exhibit a steeper slope ~ 0.15 days after the burst, indicative of a jet break. The timing of the jet break combined with the total gamma-ray energy of the burst constrains the opening angle of the jet to be 2.5° . We derive an empirical ‘time-lag’ redshift from the BAT data of $\hat{z} = 0.69 \pm 0.02$, in good agreement with the spectroscopic redshift of 0.61.

Prior to the jet break, the X-ray data can be modelled by a simple power law with index $\alpha = -1.2$. However after 300 s the X-ray flux brightens by about 30% compared to the power-law fit. The optical/UV data have a more complex decay, with evidence of a rapidly falling reverse shock component that dominates in the first minute or so, giving way to a flatter forward shock component at later times. The multiwavelength X-ray/UV/Optical spectrum of the afterglow shows evidence for migration of the electron cooling frequency through the optical range within 25000s. The measured temporal decay and spectral indices in the X-ray and optical/UV regimes compare favourably with the standard fireball model for Gamma-ray bursts assuming expansion into a constant density interstellar medium.

Subject headings: astrometry - galaxies: distances and redshifts - gamma rays: bursts - shock waves - X-rays: individual (GRB 050525a)

1. Introduction

The observation of Gamma-ray bursts has entered a new era with the launch of the Swift observatory (Gehrels et al. 2004). Swift provides rapid notification of GRB triggers to the ground using its sensitive Burst Alert Telescope (BAT; Barthelmy et al. 2005), and can make panchromatic observations of the burst and its afterglow by bringing its narrow field X-ray Telescope (XRT; Burrows et al. 2005a) and UltraViolet/Optical Telescope (UVOT; Roming et al. 2005) to bear within about 1 minute of the burst going off.

In this paper we describe Swift observations of GRB050525a, the first bright, low-redshift burst to have been observed with Swift with both its narrow field instruments. This has resulted in the most complete multiwavelength description of the early evolution of a burst afterglow yet obtained. We describe the light curve decay in the X-ray and optical/UV bands, and compare these with the predictions of theoretical models. We also consider how the multiwavelength spectrum of the burst afterglow evolves with time, making use of the simultaneous X-ray/UV/optical coverage. We combine the measurements of the afterglow properties with the well constrained measurements of the prompt Gamma-ray emission to constrain the geometry of the burst emission. We present an analysis of the prompt gamma-

ray emission in section 2.1. This is followed by an analysis of the time evolution and spectrum of the X-ray data in section 2.2, adding to this the optical and ultraviolet data in section 2.3 to build up the multiwavelength picture. The results are discussed in section 3.

2. Observations and Analysis

2.1. BAT

At 00:02:53.26 UT, the *Swift* Burst Alert Telescope (BAT) triggered and located on-board GRB050525a (trigger #130088). The BAT location calculated on-board was RA, DEC 278.144, +26.340 (J2000) with an uncertainty of 4 arcmin (radius, 3σ , including estimated systematic uncertainty). This was later refined (see Figure 1) to 278.140, +26.344 \pm 0.5' (95% containment, the position corresponding to 18h 32m 34s, +26d 20' 38") using the full data set downloaded through the Malindi groundstation \sim 1 hour after the burst. The refined position is 26 arcsec from the on-board location and 21 arcsec from the UVOT location. The burst was 28° off the BAT bore sight (85% coded) and was 148σ in the image-domain full data set. The spacecraft completed the automated slew to the burst at 00:04:58 UT (75 sec after the trigger), and XRT and UVOT began their standard follow-up observation sequences.

Figure 2 shows the BAT light curves in the 4 standard BAT energy bands. The burst was very bright and was detected in all 4 energy bands with a peak rate of \sim 80,000 cts s $^{-1}$. The burst has two main peaks with several smaller peaks within the main structure. The lag between the lightcurves in the 100–350 keV and the 25–50 keV bands is $\tau = 0.124 \pm 0.006$ s (the high energy band leads the low energy band). The total duration was \sim 12 s (T_{90} is 8.8 ± 0.5 s). The successful trigger criterion for this burst was in the 25–100 keV band with a duration of 64 msec.

Another very bright burst occurred \sim 2800 s later (GRB050525B; Golenetskii et al. 2005). This was outside the field-of-view (FOV) of INTEGRAL's IBIS instrument whereas GRB 050525A was inside the IBIS FOV. Thus we can be confident that this second burst was not associated with GRB 050525A (Mereghetti et al. 2005).

Because the burst was bright, the burst spectrum was well determined using BAT. Table 1 summarizes the spectral fits to the entire burst (12.80 s) and to the peak 1 s, with 90% confidence limits. The BAT response matrices are still under development, and consequently an additional systematic 1% uncertainty was added to the statistical uncertainty. We fit the

energy spectra with three nested models¹: a power law $F(E) \propto E^\beta$; a power law with an exponential cutoff $F(E) \propto E^\beta \exp[-E/E_0]$; and the ‘Band’ model (Band et al. 1993), a low energy power law with an exponential cutoff that transitions into a high energy power law $F(E) \propto E^{\beta_2}$. The peak energy $E_p = (1 + \beta)E_0$ is both physically more relevant and less correlated with β than E_0 ; E_p is the energy of the peak of $E F(E) \propto \nu f_\nu$. The power law with an exponential cutoff is the same as the Band model with $\beta = -\infty$, and the power law model is the same as the other two models with $E_0 = \infty$.

As can be seen from these fits, the power law fit is definitely inferior to the other two spectral models, and these two spectral models are equivalent since the transition to the high energy power law at $E_b = (\beta - \beta_2)E_0 = (\beta - \beta_2)E_0/(\beta + 2)$ is above 150 keV (the energy of the highest PHA channel fit); indeed, for the observed β and E_p values, the fits are insensitive to $\beta_2 < -2.5$.

Konus-Wind (Golenetskii et al. 2005) and *INTEGRAL* (Gotz et al. 2005) both detected GRB050525a. Golenetskii et al. (2005) fit the Konus-Wind 20 keV to 1 MeV spectrum for the entire burst with a power law with an exponential cutoff model and find $\beta = -0.10 \pm 0.05$, and $E_p = 84.1 \pm 1.7$ keV, consistent with the *Swift* fit.

The spectral fits can be integrated over energy and time to give a fluence $S(15\text{--}350 \text{ keV}) = (2.01 \pm 0.05) \times 10^{-5} \text{ erg cm}^{-2}$ and a peak flux of $P = (15\text{--}350 \text{ keV}) = 47.7 \pm 1.2 \text{ photons cm}^{-2} \text{ s}^{-1}$. Using the observed redshift of $z = 0.606$ (Foley et al. 2005), the spectral fits and a standard cosmology ($\Omega_m = 0.3$, $\Omega_\Lambda = 0.7$, and $H_0 = 70 \text{ km s}^{-1} \text{ Mpc}^{-1}$), we find $E_{\text{iso}} = 2.3 \times 10^{52} \text{ erg}$ and $L_{\text{iso}} = 7.8 \times 10^{51} \text{ erg s}^{-1}$. These two derived quantities are the total energy and peak luminosity that would have been radiated if the observed flux were emitted isotropically. As will be discussed below (section 3) in considering the possible jet break, the emission was most likely beamed and the actual emitted energy and luminosity were consequently smaller. Using the redshift, the peak energies in the burst frame are $E_{\text{pp}} = 164.5 \pm 11.6$ keV for the peak of the lightcurve and $E_{\text{pt}} = 126.6 \pm 5.5$ keV for the entire burst.

2.2. XRT data

The XRT observations started on 2005 May 25 at 00:04:08 UT, 75 seconds after the trigger. The XRT was undergoing engineering tests at the time of the burst and the Auto State was disabled. A sequence of 3 frames in Photon Counting (PC) mode were taken first,

¹We use the notation β here and throughout the paper to denote the power law index of the energy spectrum of the source.

Table 1. BAT Spectral Fits

Parameter	Entire Burst			Peak Flux		
	Power Law ^a	Power Law, Cutoff ^b	Band Model ^c	Power Law ^a	Power Law, Cutoff ^b	Band Model ^c
β^d	-0.782 ^e	$0.013^{+0.113}_{-0.116}$	$0.013^{+0.113}_{-0.116}$	-0.420 ^e	$0.448^{+0.136}_{-0.140}$	$-0.448^{+0.140}_{-0.136}$
β_2^f	—	—	$-7.839^{+6.400}_{-1.161}$	—	—	$-8.268^{+7.137}_{-0.732}$
E_p^g	—	$78.8^{+3.9}_{-3.1}$	$78.8^{+3.7}_{-3.1}$	—	$102.4^{+7.1}_{-6.3}$	$102.4^{+8.1}_{-6.3}$
Norm	$7.15^{e,h}$	$14.2^{+5.9}_{-4.2}$	$15.0^{+1.65}_{-1.45}$ h	$19.35^{e,h}$	$7.62^{+3.91}_{-2.65}$ i	$44.00^{+6.05}_{-5.20}$ h
χ^2/dof	181.72/57	15.17/56	15.17/56	169.76/57	31.59/56	31.59/55

^aPower law model, $F(E) \propto E^\beta$.

^bPower law with an exponential cutoff, $F(E) \propto E^\beta \exp[-E/E_0]$.

^cBand model (Band et al. 1993), a low energy power law with an exponential cutoff transitioning to a high energy power law $F(E) \propto E^{\beta_2}$.

^dThe low energy spectral index.

^eFit too poor to produce uncertainty range.

^fThe high energy spectral index.

^gThe energy of the peak of $EN(E) \propto \nu f_\nu$, and $E_p = (2 + \beta)E_0$.

^hThe normalization of the spectrum at 50 keV, in $\text{keV cm}^{-2} \text{ s}^{-1} \text{ keV}^{-1}$.

ⁱThe normalization of the spectrum at 1 keV, in $\text{keV cm}^{-2} \text{ s}^{-1} \text{ keV}^{-1}$.

between T+75s to T+83s. These early PC mode data suffer from severe pile-up because of the brightness of the source, and have been excluded from the analysis.

Shortly afterward the instrument was put into Auto State and a 2.5 s exposure in Image mode was taken starting at 00:04:58 UT, 125 seconds after the BAT burst trigger. A bright X-ray source was found near the center of the field of view. The refined X-ray coordinates are RA(J2000) = $18^{\text{h}}32^{\text{m}}32^{\text{s}}.6$ and Dec(J2000) = $26^{\circ}20'18''$, with an estimated positional uncertainty of 6 arc seconds (90% confidence level). The XRT coordinates are 4 arc seconds from the UVOT position of the optical counterpart (see below).

Following the automatic sequence of readout modes, designed to avoid any pile-up effect, the instrument was configured in the Photodiode (PD) readout mode starting from 00:05:01 UT (T+128 s). Due to the engineering tests mentioned above, the instrument remained in PD mode until 00:20:21 UT (T+1048 s) even when the afterglow brightness was below the nominal flux threshold used for this mode.

Data in PC mode, the most sensitive XRT operational mode, were taken starting at 01:40:32 UT until 11:39:11 UT. The GRB050525a field was re-observed in PC mode on several occasions up to late June 2005.

2.2.1. *Temporal analysis*

For the PD mode, events for the temporal analysis were selected in the 0.4–4.5 keV energy band to avoid contamination from the calibration sources. The standard grade selection for this mode (0–5) was used. The count rate was converted to unabsorbed 2–10 keV flux using the best fit spectral model (see below).

For PC data, events were selected in the 0.3–10 keV band and grades 0–12 were used in the analysis. Furthermore, since 2-D spatial information is available for this mode, photons within a circle of 10 pixel (~ 24 arcsec) radius, which encloses about 80% of the PSF at 1.5 keV, were extracted, centered on the source position. The background was estimated from a nearby source-free circular region with 50 pixel radius. Again, the count rate in the 0.3–10 keV band was converted to unabsorbed 2–10 keV flux using the best fit spectral model.

Table 2. XRT 2-10 keV flux

T(mid) ^a	Exposure	Flux ^b
	(seconds)	
133.0	5.	122.7 ± 5.7
143.0	5.	109.5 ± 5.4
153.0	5.	101.4 ± 5.2
163.0	5.	92.0 ± 4.9
173.0	5.	86.8 ± 4.8
183.0	5.	83.7 ± 4.7
193.0	5.	77.2 ± 4.5
203.0	5.	69.4 ± 4.3
213.0	5.	69.2 ± 4.3
223.0	5.	62.4 ± 4.1
233.0	5.	65.0 ± 4.1
243.0	5.	57.2 ± 3.9
253.0	5.	54.6 ± 3.8
263.0	5.	54.3 ± 3.8
278.0	10.	50.8 ± 2.6
298.0	10.	49.8 ± 2.6
318.0	10.	45.4 ± 2.5
338.0	10.	45.5 ± 2.5
358.0	10.	46.9 ± 2.5
378.0	10.	40.2 ± 2.3
398.0	10.	41.7 ± 2.4
418.0	10.	39.4 ± 2.3
438.0	10.	39.9 ± 2.3
458.0	10.	34.8 ± 2.2
478.0	10.	31.9 ± 2.1
498.0	10.	31.5 ± 2.1
518.0	10.	32.5 ± 2.1
538.0	10.	27.4 ± 1.9
558.0	10.	32.4 ± 2.1
578.0	10.	29.8 ± 2.0
598.0	10.	28.5 ± 2.0
618.0	10.	29.1 ± 2.0
638.0	10.	24.8 ± 1.8
658.0	10.	27.3 ± 1.9
678.0	10.	24.6 ± 1.8
708.0	20.	24.2 ± 1.3

Table 2—Continued

T(mid) ^a	Exposure (seconds)	Flux ^b
748.0	20.	20.4 ± 1.2
788.0	20.	19.8 ± 1.2
828.0	20.	19.0 ± 1.1
868.0	20.	16.3 ± 1.1
908.0	20.	18.5 ± 1.1
948.0	20.	17.6 ± 1.1
988.0	20.	16.3 ± 1.1
1028.0	20.	15.5 ± 1.4
6009.0	150.	1.072 ± 0.134
6309.0	150.	1.331 ± 0.153
6609.0	150.	0.987 ± 0.126
6909.0	150.	1.010 ± 0.152
11809.0	350.	0.560 ± 0.056
12509.0	350.	0.482 ± 0.052
18109.0	350.	0.331 ± 0.052
23859.0	2000.	0.173 ± 0.039
27859.0	2000.	0.108 ± 0.028
35859.0	2000.	0.079 ± 0.021
81459.0	5400.	0.0361 ± 0.0088
99102.0	11850.	0.0273 ± 0.0078
165485.0	22000.	0.0080 ± 0.0016
412515.0	42000.	0.0013 ± 0.0006

^atime since trigger (s)^bflux in units of 10^{-11} erg cm $^{-2}$ s $^{-1}$ 2-10 keV

Table 3. UVOT multicolor data

T(mid) ^a	Exposure	Mag	Flux ^b
V filter	(seconds)		
66.0	1.	13.21 ± 0.24	189.8 ± 41.2
67.0	1.	12.90 ± 0.23	254.0 ± 53.6
68.0	1.	12.86 ± 0.23	263.3 ± 55.5
69.0	1.	13.01 ± 0.23	227.9 ± 48.5
70.0	1.	12.97 ± 0.23	236.3 ± 50.1
71.0	1.	13.31 ± 0.23	172.8 ± 34.0
72.0	1.	13.13 ± 0.23	204.3 ± 43.9
73.0	1.	13.01 ± 0.23	227.9 ± 48.5
78.0	5.	13.13 ± 0.10	204.3 ± 19.6
83.0	5.	13.26 ± 0.10	181.5 ± 17.7
88.0	5.	13.18 ± 0.10	195.5 ± 18.9
93.0	5.	13.24 ± 0.11	185.6 ± 18.1
98.0	5.	13.25 ± 0.11	184.2 ± 17.9
103.0	5.	13.51 ± 0.11	144.9 ± 14.7
108.0	5.	13.44 ± 0.11	154.4 ± 15.5
113.0	5.	13.67 ± 0.11	124.7 ± 13.0
118.0	5.	13.48 ± 0.11	148.4 ± 15.0
123.0	5.	13.62 ± 0.11	130.2 ± 13.5
128.0	5.	13.86 ± 0.12	104.2 ± 11.4
133.0	5.	13.70 ± 0.11	121.5 ± 12.8
138.0	5.	13.83 ± 0.12	107.2 ± 11.6
143.0	5.	13.81 ± 0.12	109.2 ± 11.8
148.0	5.	13.84 ± 0.12	106.2 ± 11.5
153.0	5.	13.87 ± 0.12	103.2 ± 11.3
158.0	5.	14.06 ± 0.12	87.1 ± 10.0
163.0	5.	14.00 ± 0.12	91.7 ± 10.3
168.0	5.	14.01 ± 0.12	90.8 ± 10.3
173.0	10.	14.08 ± 0.13	83.3 ± 10.6
258.0	10.	14.64 ± 0.14	49.8 ± 6.8
342.0	10.	14.79 ± 0.15	43.3 ± 6.4
426.0	10.	15.22 ± 0.17	29.2 ± 4.9
511.0	10.	15.47 ± 0.19	23.2 ± 4.4
595.0	10.	16.06 ± 0.24	13.4 ± 3.3
680.0	10.	15.83 ± 0.22	16.6 ± 3.7
764.0	10.	16.06 ± 0.25	13.4 ± 3.5

Table 3—Continued

T(mid) ^a	Exposure (seconds)	Mag	Flux ^b
849.0	10.	15.78 ± 0.22	17.4 ± 3.9
933.0	10.	15.85 ± 0.24	16.3 ± 4.0
1243.0	100.	16.34 ± 0.15	10.4 ± 1.5
18575.0	156.	18.15 ± 0.41	2.0 ± 0.9
22163.0	580.	19.10 ± 0.27	0.8 ± 0.2
35638.0	750.	18.86 ± 0.27	1.0 ± 0.3
49320.0	4982.	> 20.62	< 0.2
971360.0	33800.	> 22.09	< 0.1
1171176.0	6081.	> 21.16	< 0.1
B filter			
229.0	10.	14.79 ± 0.12	72.2 ± 8.4
313.0	10.	15.19 ± 0.12	49.9 ± 5.8
397.0	10.	15.51 ± 0.13	37.2 ± 4.7
482.0	10.	15.63 ± 0.14	33.3 ± 4.6
571.0	10.	15.70 ± 0.14	31.2 ± 4.3
651.0	10.	16.13 ± 0.16	21.0 ± 3.3
735.0	10.	16.03 ± 0.16	23.0 ± 3.7
820.0	10.	16.56 ± 0.20	14.1 ± 2.9
904.0	10.	16.44 ± 0.20	15.8 ± 3.2
1034.0	100.	16.61 ± 0.11	13.5 ± 1.4
12671.0	390.	18.59 ± 0.18	2.2 ± 0.4
16182.0	190.	18.69 ± 0.17	2.0 ± 0.3
30031.0	388.	19.82 ± 0.52	0.7 ± 0.4
33898.0	900.	20.84 ± 0.45	0.3 ± 0.1
45468.0	896.	> 20.70	< 0.3
62549.0	6513.	> 21.55	< 0.1
U filter			
215.0	10.	13.70 ± 0.18	110.3 ± 19.9
299.0	10.	14.08 ± 0.18	77.8 ± 14.0
419.0	10.	14.47 ± 0.19	54.3 ± 10.4
468.0	10.	14.71 ± 0.19	43.5 ± 8.3
552.0	10.	14.97 ± 0.20	34.3 ± 6.9
637.0	10.	15.01 ± 0.20	33.0 ± 6.7
721.0	10.	15.14 ± 0.20	29.3 ± 5.9
805.0	10.	15.46 ± 0.21	21.8 ± 4.7
890.0	10.	15.29 ± 0.21	25.5 ± 5.4

Table 3—Continued

T(mid) ^a	Exposure	Mag	Flux ^b
	(seconds)		
975.0	10.	15.32 ± 0.22	24.8 ± 5.6
12019.0	900.	17.66 ± 0.17	2.9 ± 0.5
28664.0	194.	18.85 ± 0.30	1.0 ± 0.3
29380.0	900.	18.79 ± 0.20	1.0 ± 0.2
41040.0	758.	19.99 ± 0.54	0.3 ± 0.2
52994.0	780.	> 19.68	< 0.4
128928.0	1548.	> 20.05	< 0.3
UVW1 (260 nm) filter			
202.0	10.	13.61 ± 0.07	162.8 ± 10.4
286.0	10.	14.18 ± 0.09	96.3 ± 8.0
370.0	10.	14.77 ± 0.12	56.2 ± 6.2
455.0	10.	15.10 ± 0.14	41.5 ± 5.3
539.0	10.	15.22 ± 0.15	37.0 ± 5.1
624.0	10.	15.26 ± 0.15	35.6 ± 4.9
708.0	10.	15.22 ± 0.15	36.9 ± 5.1
792.0	10.	15.88 ± 0.21	20.1 ± 3.8
877.0	10.	16.15 ± 0.24	15.7 ± 3.5
961.0	10.	15.76 ± 0.20	22.6 ± 4.1
6761.0	638.	17.33 ± 0.06	5.3 ± 0.3
28111.0	900.	19.49 ± 0.19	0.7 ± 0.1
40585.0	900.	20.33 ± 0.39	0.3 ± 0.1
52100.0	898.	> 21.05	< 0.3
63738.0	900.	> 21.20	< 0.3
UVM2 (220 nm) filter			
187.0	10.	13.54 ± 0.10	218.9 ± 20.0
272.0	10.	14.32 ± 0.14	106.8 ± 14.1
356.0	10.	14.60 ± 0.16	82.4 ± 12.4
440.0	10.	14.94 ± 0.19	60.3 ± 10.7
525.0	10.	15.84 ± 0.30	26.4 ± 7.2
609.0	10.	14.90 ± 0.19	62.4 ± 10.8
694.0	10.	15.18 ± 0.21	48.3 ± 9.4
778.0	10.	15.51 ± 0.26	35.9 ± 8.5
863.0	10.	15.57 ± 0.26	33.8 ± 8.1
947.0	10.	15.66 ± 0.27	31.2 ± 7.6
5984.0	900.	17.10 ± 0.06	8.2 ± 0.4
24007.0	864.	18.96 ± 0.19	1.5 ± 0.3

The background subtracted 2–10 keV light curve in the time interval $T+128\text{ s} - T+1048\text{ s}$ (PD mode) is shown in Figure 3. The X-ray afterglow of GRB 050525 is clearly fading. The early afterglow decay was first fitted with a single power-law model, resulting in a best fit decay index $\alpha = -0.95 \pm 0.03$, with $\chi_r^2 = 1.17$ (42 dof). Inspection of the residuals to the best fit model suggests that a flattening of the decay curve or a re-brightening of the source occurs at ~ 300 seconds after the trigger. A better fit is provided by a broken power law model with slopes α_1, α_2 and a break at t_b . This model gave $\chi_r^2 = 0.98$ (40 dof), with best fit parameters $\alpha_1 = -1.23^{+0.03}_{-0.02}$, $\alpha_2 = -0.91$ and $t_b = 203\text{ s}$.

Again, however, the residuals suggest systematic deviations from this model. We thus tried a broken power law with two temporal breaks. This model provided a very good fit to the data, with $\chi_r^2 = 0.72$ (38 dof) and is plotted in Figure 3 as a solid line. The best fit parameters are $\alpha_1 = -1.19$, $t_b^1 = 282\text{ s}$, $\alpha_2 = -0.30$, $t_b^2 = 359\text{ s}$, and $\alpha_3 = -1.02$.

Next, we fitted the X-ray data taken in PC mode at times more than 5000 s after the trigger. We first used a single power-law model, obtaining a best fit decay index $\alpha = -1.51 \pm 0.07$, with $\chi_r^2 = 1.40$ (12 dof). The poor fit is the result of a clear steepening of the light curve with time. We thus tried a broken power law model. The model provided a very good fit with $\chi_r^2 = 0.97$ (10 dof) and best fit parameters $\alpha_1 = -1.16$, $\alpha_2 = -1.62$ and $t_b = 13177\text{ s}$.

Finally, we tried fitting the total light curve derived from the combined PD and PC mode data (see Figure 4). We find that the power law fit to the pre-brightening PD mode data ($T < 280\text{ s}$) extrapolates well to the pre-break PC mode data. Moreover the slope of the decay before 280 s agrees well with that of the PC mode data before the 13ks break. In contrast, if we extrapolate the post brightening PD mode data to later times using the best fit slope, a significant excess is predicted compared with the measured PC mode data. To join the post brightening PD mode data to the PC mode data requires a model with at least two temporal breaks, which are not constrained because of the intervening gap in X-ray coverage. We conclude that the brightening at about 280 s in the PD mode data represents a flare in the X-ray flux, possibly similar to those seen at early times in other bursts (Burrows et al 2005b; Piro et al. 2005), and that the flux returns to the pre-flare decay curve prior to the start of our PC mode data.

We thus fit the combined PD and PC mode data excluding PD data at times $t > T+288\text{ s}$ (green circles in Figure 4). A broken power law model provided a good fit (solid line of Figure 4), with $\chi_r^2 = 0.50$ (25 dof) and best fit parameters $\alpha_1 = -1.20 \pm 0.03$, $\alpha_2 = -1.62^{+0.11}_{-0.16}$ and $t_b = 13726^{+7469}_{-5123}\text{ s}$. The break time is thus ~ 3.8 hours.

The complete XRT data are recorded in Table 2.

Table 3—Continued

T(mid) ^a	Exposure	Mag	Flux ^b
	(seconds)		
39683.0	897.	19.72 ± 0.30	0.7 ± 0.2
51257.0	900.	20.34 ± 0.48	0.4 ± 0.2
74798.0	931.	> 21.59	< 0.6
UVW2 (198 nm) filter			
245.0	10.	14.69 ± 0.11	88.4 ± 9.5
329.0	10.	15.30 ± 0.16	50.2 ± 7.2
413.0	10.	15.13 ± 0.14	58.6 ± 7.7
498.0	10.	15.60 ± 0.18	38.2 ± 6.4
582.0	10.	15.22 ± 0.15	54.3 ± 7.5
666.0	10.	15.80 ± 0.20	31.7 ± 5.8
751.0	10.	15.72 ± 0.19	34.3 ± 5.9
835.0	10.	16.43 ± 0.27	17.8 ± 4.5
920.0	10.	16.21 ± 0.25	21.8 ± 4.9
1140.0	100.	16.35 ± 0.08	19.1 ± 1.5
17973.0	882.	18.99 ± 0.13	1.7 ± 0.2
34806.0	900.	20.05 ± 0.25	0.6 ± 0.1
52162.0	1800.	> 21.76	< 0.3

^atime since trigger (s)

^bflux in units of 10^{-16} erg cm $^{-2}$ s $^{-1}$ Å $^{-1}$

Table 4. UVOT White Light

T(start)	T(stop)	Exposure	V Mag ^a	V Flux ^b
	(seconds)			
93167	111189	2378	21.35 ± 0.27	0.103 ± 0.025
173859	329532	11750	22.82 ± 0.43	0.027 ± 0.010
329532	2599088	146267	> 24.11	< 0.008

^aequivalent V-band magnitude

^bequivalent V-band flux in units of 10^{-16} erg cm $^{-2}$ s $^{-1}$ Å $^{-1}$

2.2.2. Spectral analysis

The Photodiode spectrum in the time interval T+128 s to T+1048 s has been extracted in the 0.4–4.5 keV band. The spectrum was binned to ensure a minimum of 20 counts per bin and was fitted using the XSPEC package (v. 11.3.2).

An absorbed power law model fits the data well. The best fit hydrogen-equivalent column density is $N_{\text{H}} = 2.06 \pm 0.14 \times 10^{21} \text{ cm}^{-2}$ and the energy index is $\beta = -0.98 \pm 0.06$ ($\chi^2_r = 1.08$, 283 dof). Freezing N_{H} to the Galactic value ($9.0 \times 10^{20} \text{ cm}^{-2}$) and fitting a hydrogen-equivalent column density at the redshift of the GRB ($z = 0.606$) yielded $N_{\text{H}}^z = 2.4_{-0.3}^{+0.5} \times 10^{21} \text{ cm}^{-2}$, $\beta = -0.90 \pm 0.05$ with $\chi^2_r = 1.07$ (283 dof).

Events in PC mode from the time interval T+5859 s to T+41778 s were extracted from the same circular region used in the temporal analysis. A further selection on XRT event grades 0–4 (i.e. single and double pixel events) was applied to the data. Again, the spectrum was binned to ensure a minimum of 20 counts per bin. Energy channels below 0.3 keV and above 10.0 keV were excluded.

An absorbed power law model fits the PC data well ($\chi^2_r = 0.70$, 21 dof), with $N_{\text{H}} = 1.5_{-0.7}^{+0.8} \times 10^{21} \text{ cm}^{-2}$ and $\beta = -1.10_{-0.24}^{+0.27}$.

No evidence is found for evolution of the X-ray spectral shape with time (cf. Chincarini et al. 2005).

2.3. UVOT data

The Swift UVOT began taking data in the V filter ~ 65 seconds after the burst trigger, immediately after the GRB came into its field of view. After about ten seconds the spacecraft attitude had settled and UVOT began a 100s ‘finding chart’ exposure in V. Thereafter the instrument cycled through each of six color filters, V, B and U together with filters defining three ultraviolet passbands, UVW1, UVM2 & UVW2 with central wavelengths of 260nm, 220nm & 193nm respectively. The exposure duration per filter was initially 10 seconds, subsequently increasing to 100s and then 900s at predetermined times after the trigger. Data were taken in both ‘event mode’, in which the time and detector position of each individual photon is recorded, and in ‘image mode’, where the image is accumulated onboard, discarding the photon timing information within an exposure to reduce telemetry volume. At some phases of the observation both modes were operated simultaneously through different sized spatial windows that were selected in combination with the window size and the spatial binning of the image mode data so as to match the overall data volume with the available

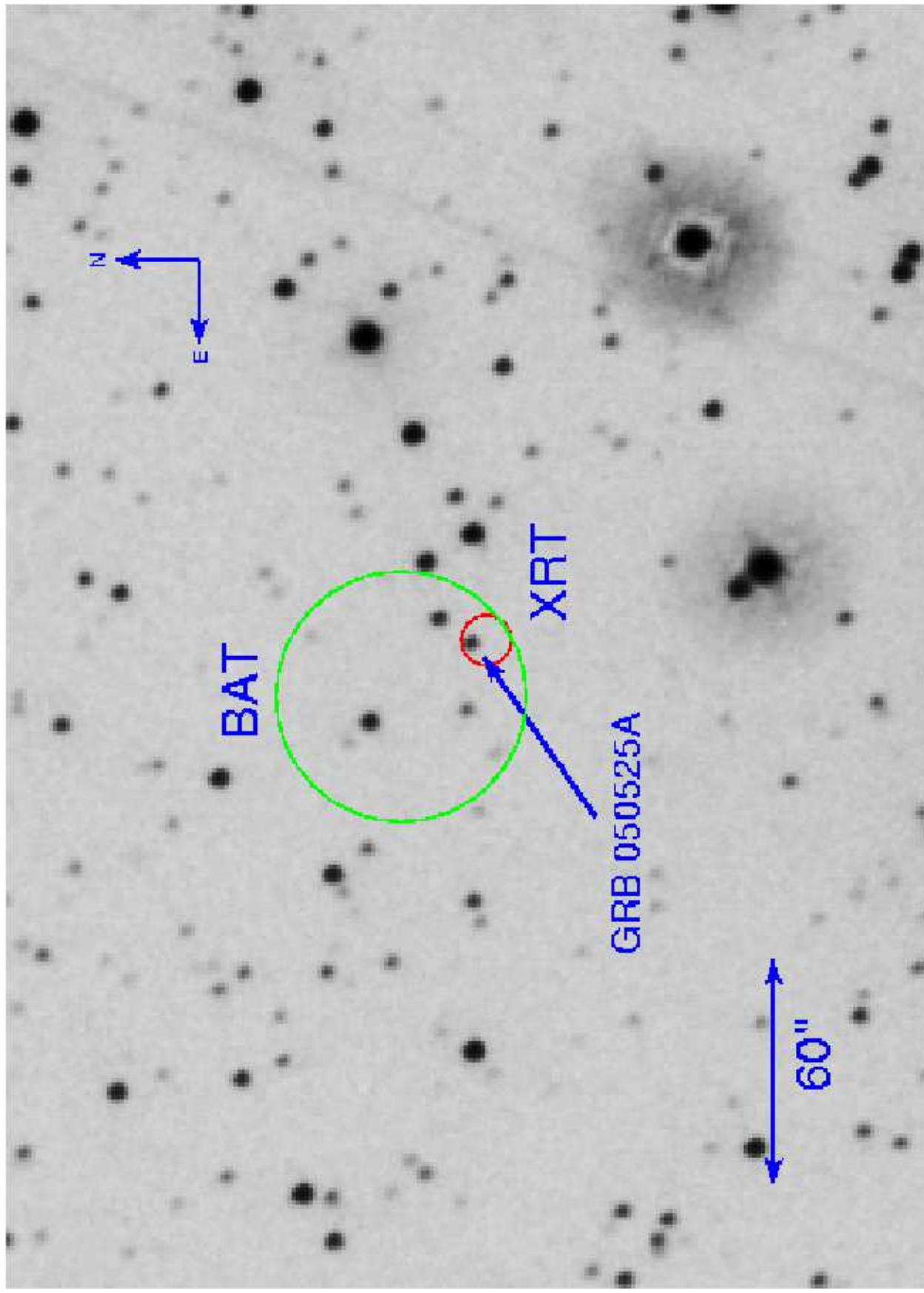


Fig. 1.— This Figure shows the field containing GRB 050525A, marking the location of

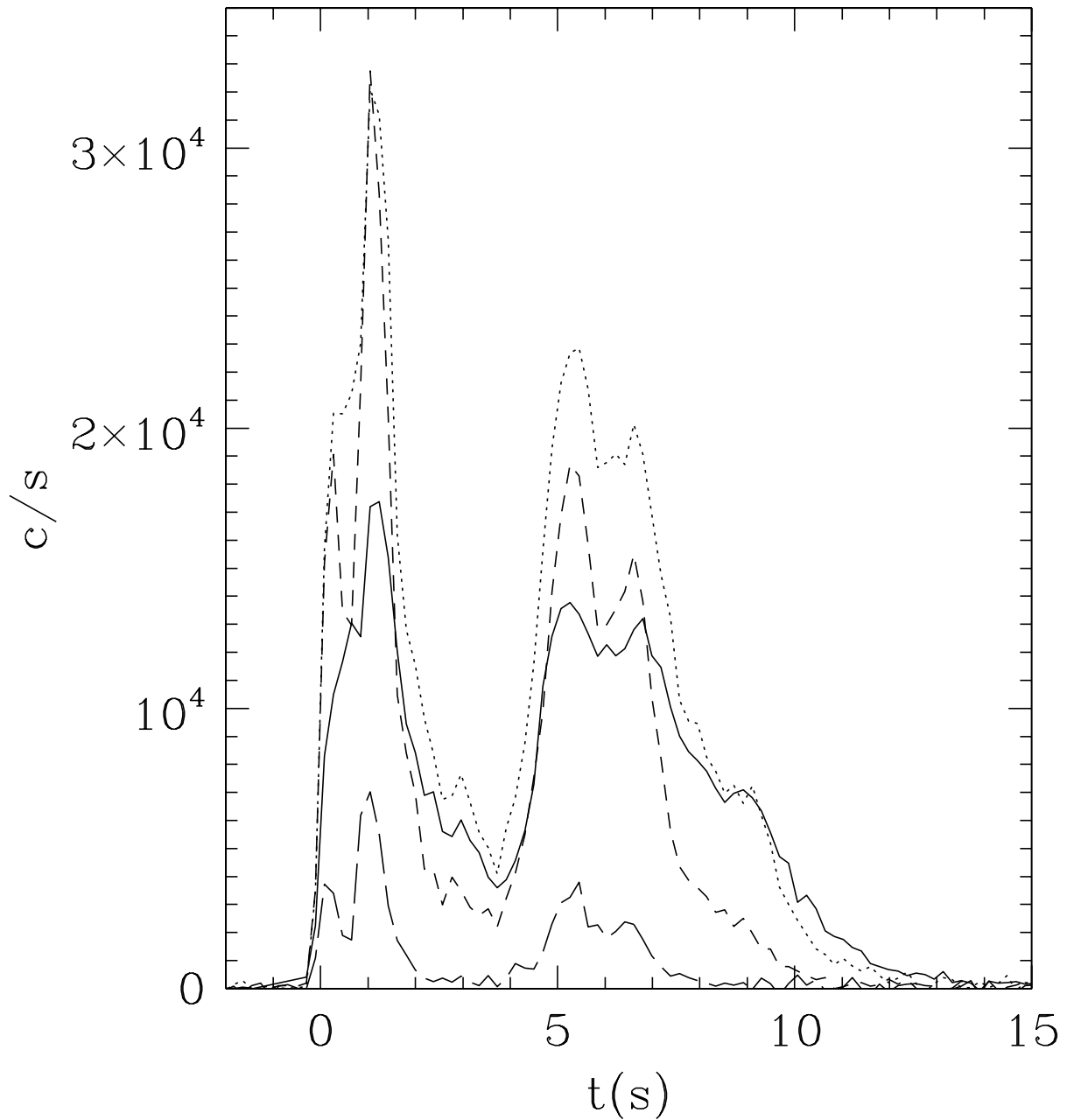


Fig. 2.— BAT lightcurve of GRB050525a in the 15-25 keV (solid), 25-50 keV (dots), 50-100 keV (short dashes), and 100-350 keV (long dashes) bands.

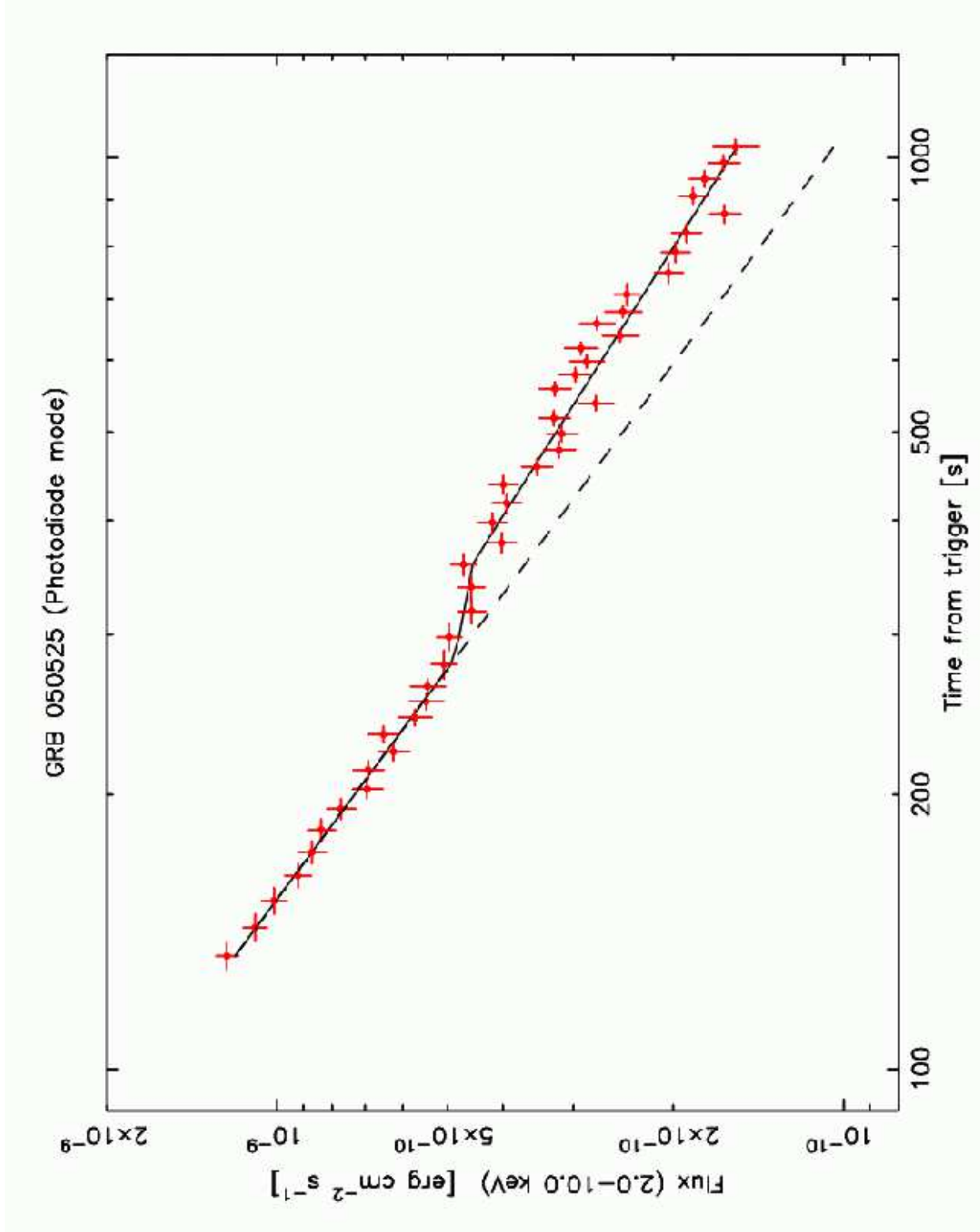


Fig. 3.— XRT decay light curve of GRB050525a taken in photodiode mode during the first ~ 1000 s after the BAT trigger. The solid line is a fit to the data with a power law model that includes two temporal breaks to different decay rates. The dashed line is an extrapolation of a simple power law fit (single slope) to the first segment of data prior to about 300 s.

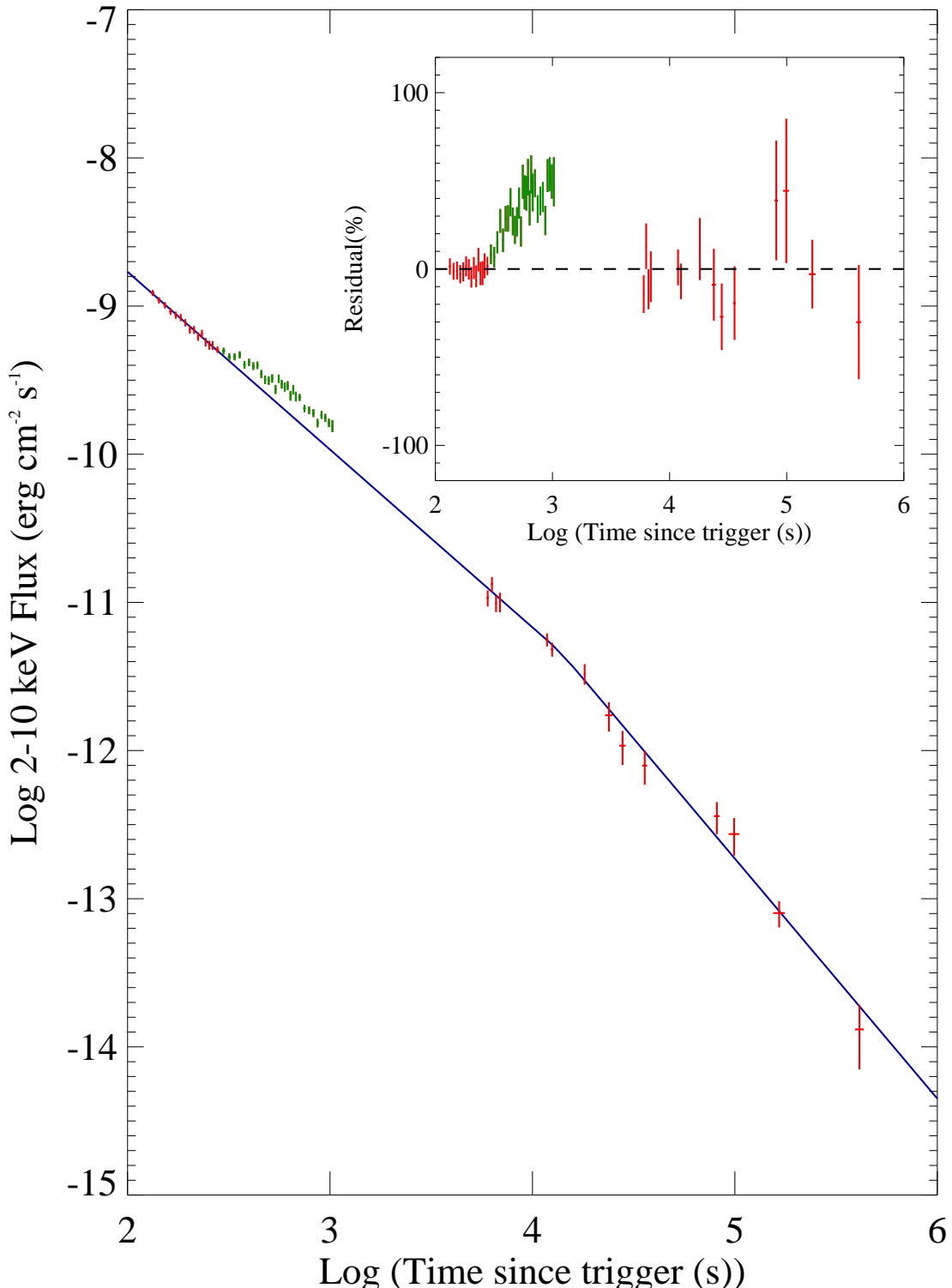


Fig. 4.— XRT decay light curve of GRB050525a including both Photodiode Mode ($T < 2000$ s) and Photon Counting Mode ($T > 2000$ s) data. The solid line is a broken power law fit to the combined data excluding those Photodiode Mode points colored green (see text). The inset shows the residuals to the two power-law fit as a percentage of the predicted flux.

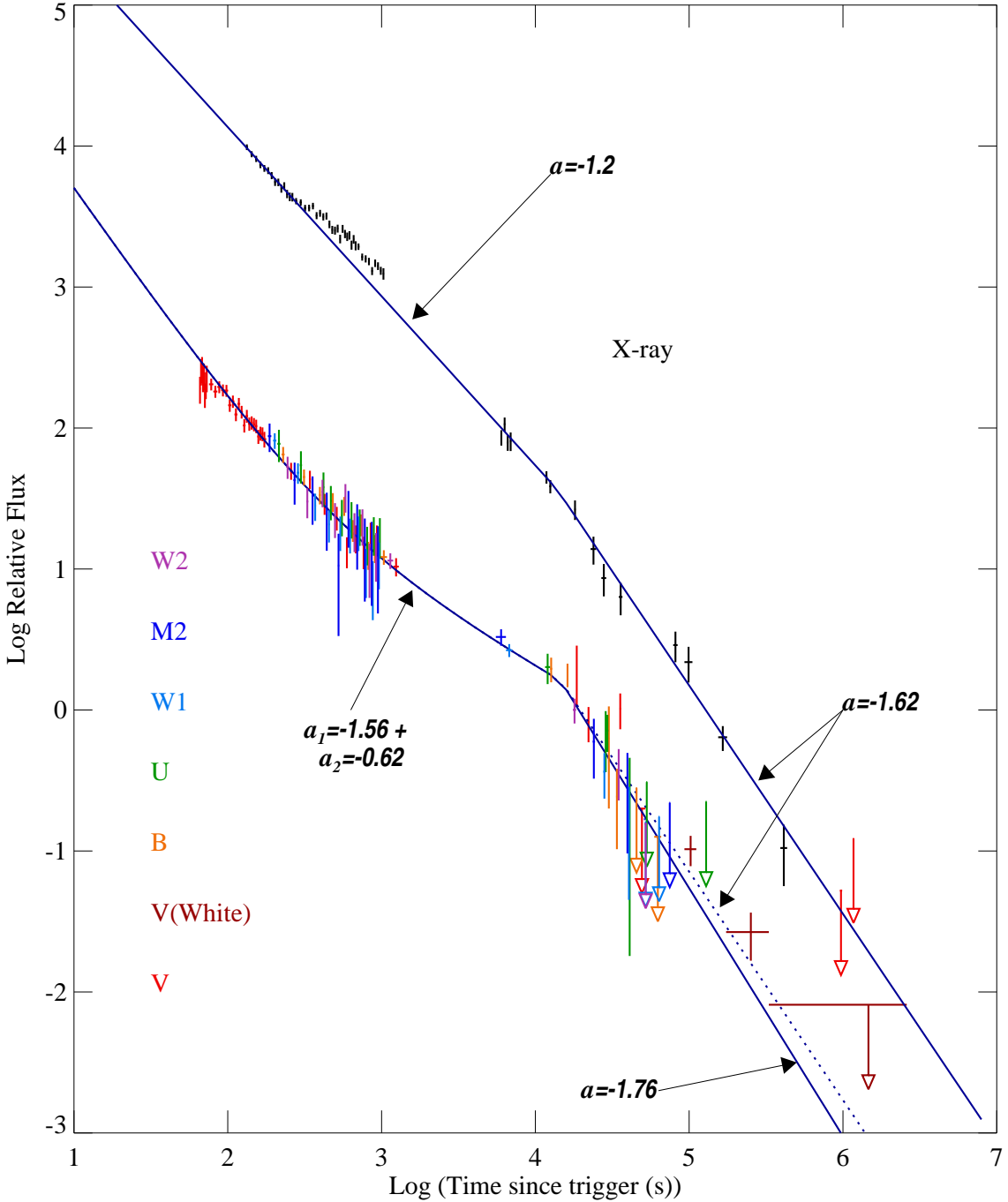


Fig. 5.— Comparison of flux decay in the X-ray and UVOT bands. The UVOT data have been normalised in the interval up to $T+1000$ s, and the data taken through different filters are distinguished by color. The best fit broken power law model is plotted through the X-ray data. The best fit double power law with break is plotted through the UVOT data (see text). The dashed line has the same post break slope as the X-ray data.

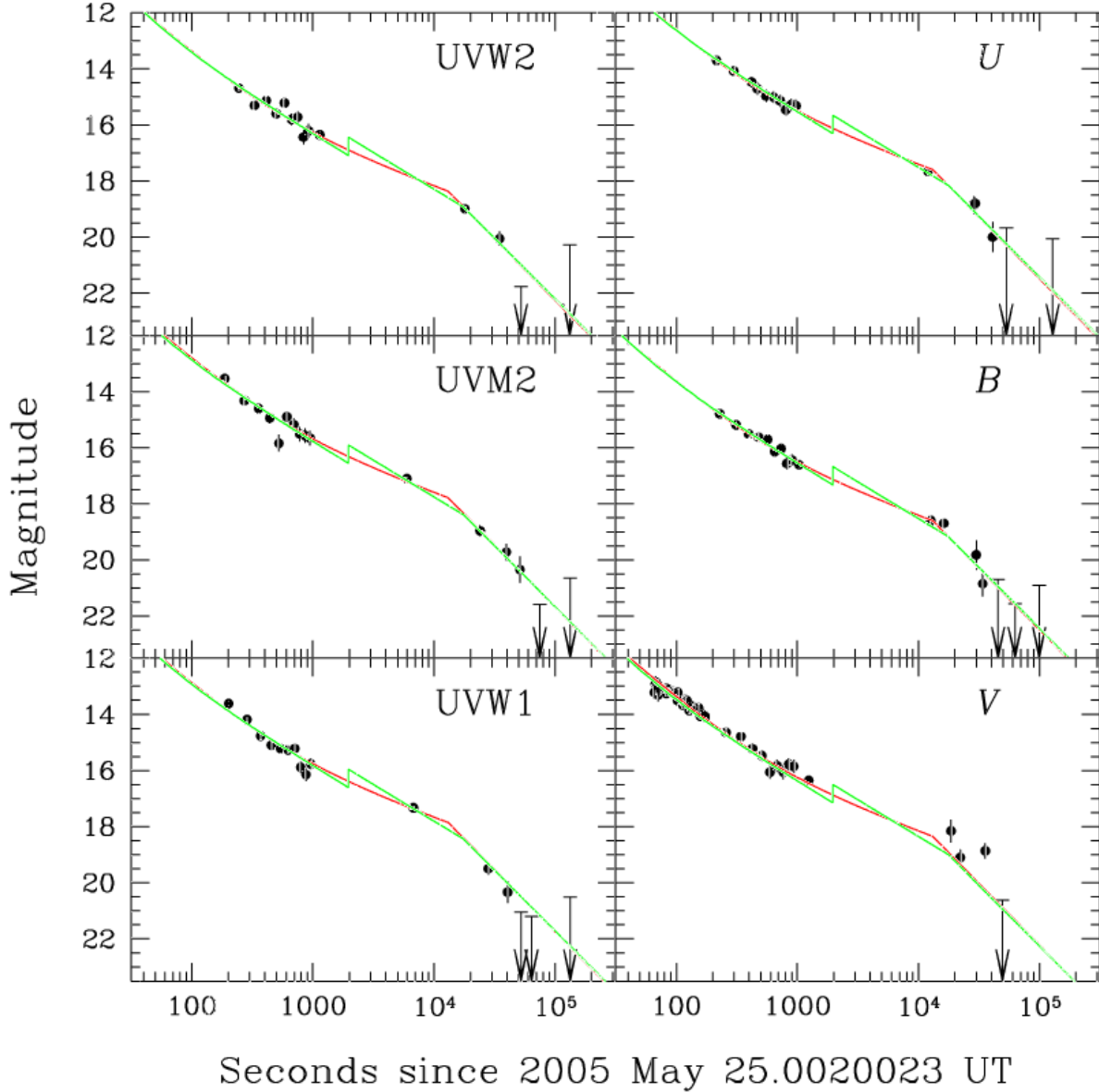


Fig. 6.— This Figure shows the photometry (solid circles) in the six UVOT broadband filters. Arrows indicate 3σ upper limits to the photometry. A model light curve (red line) with $\alpha_1 = -1.56$, $\alpha_2 = -0.62$, $\alpha_j = -1.76$, $t_t = 432$ s (7.2 min), and $t_j = 13\,133$ s (0.152 days) is shown. The green line indicates a rebrightening model with $\alpha_1 = -2.14$, $\alpha_2 = -1.04$, $\alpha_j = -1.73$, $t_t = 39$ s, and $t_j = 17\,747$ s (0.205 days). The flux has been normalized for each filter.

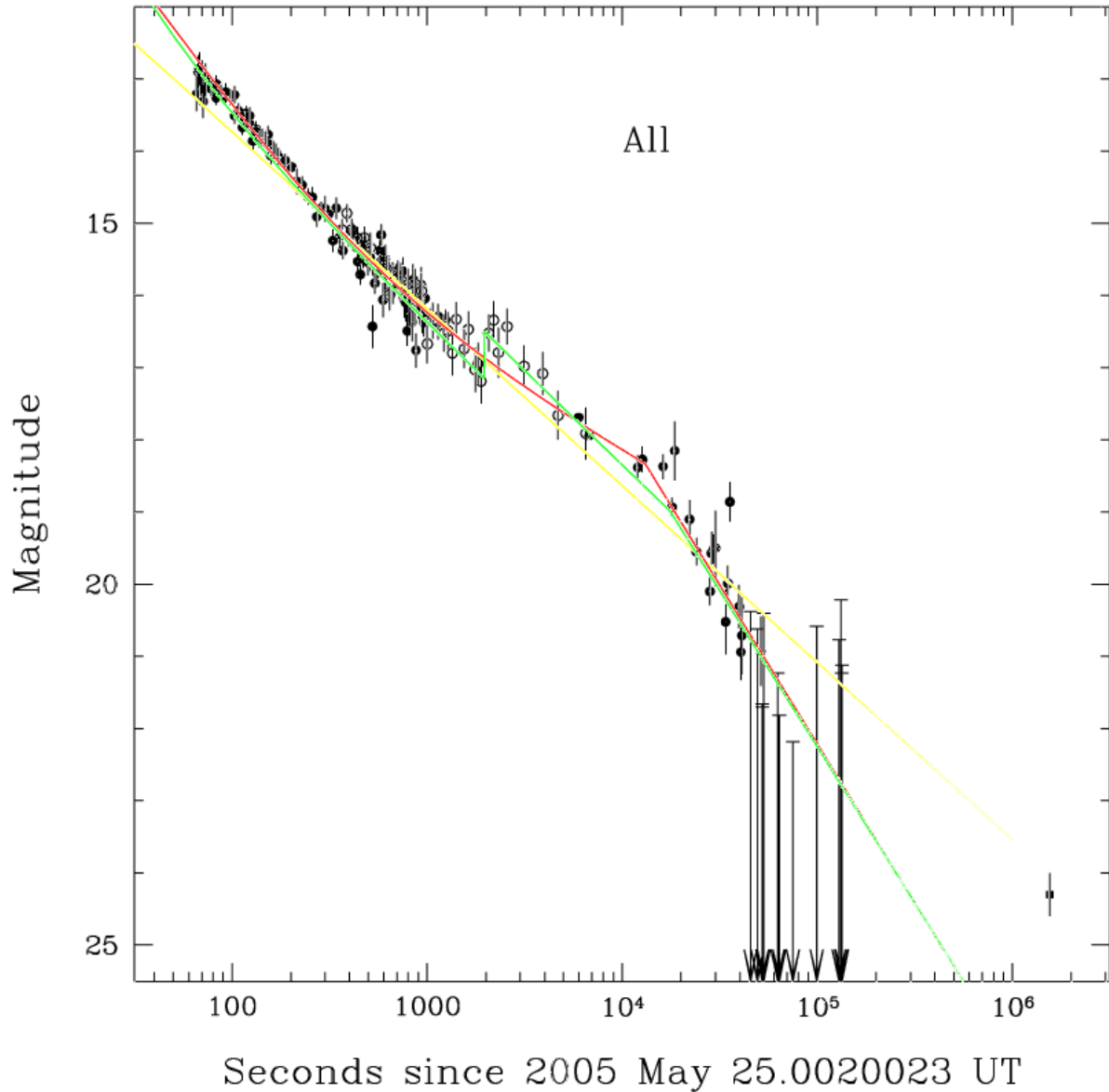


Fig. 7.— This Figure shows the UVOT photometry (solid circles) normalized so that the early time flux is the same in each filter. The red and green lines are the models from Figure 4. The yellow line is the best-fitting single power law. The open circles are the Klotz et al. (2005) data scaled to the same flux scale. The solid square is the *HST*/ACS F625W data of Soderberg et al. (2005). Note that the *HST*/ACS data point is approximately three mag brighter than the predicted afterglow magnitude.

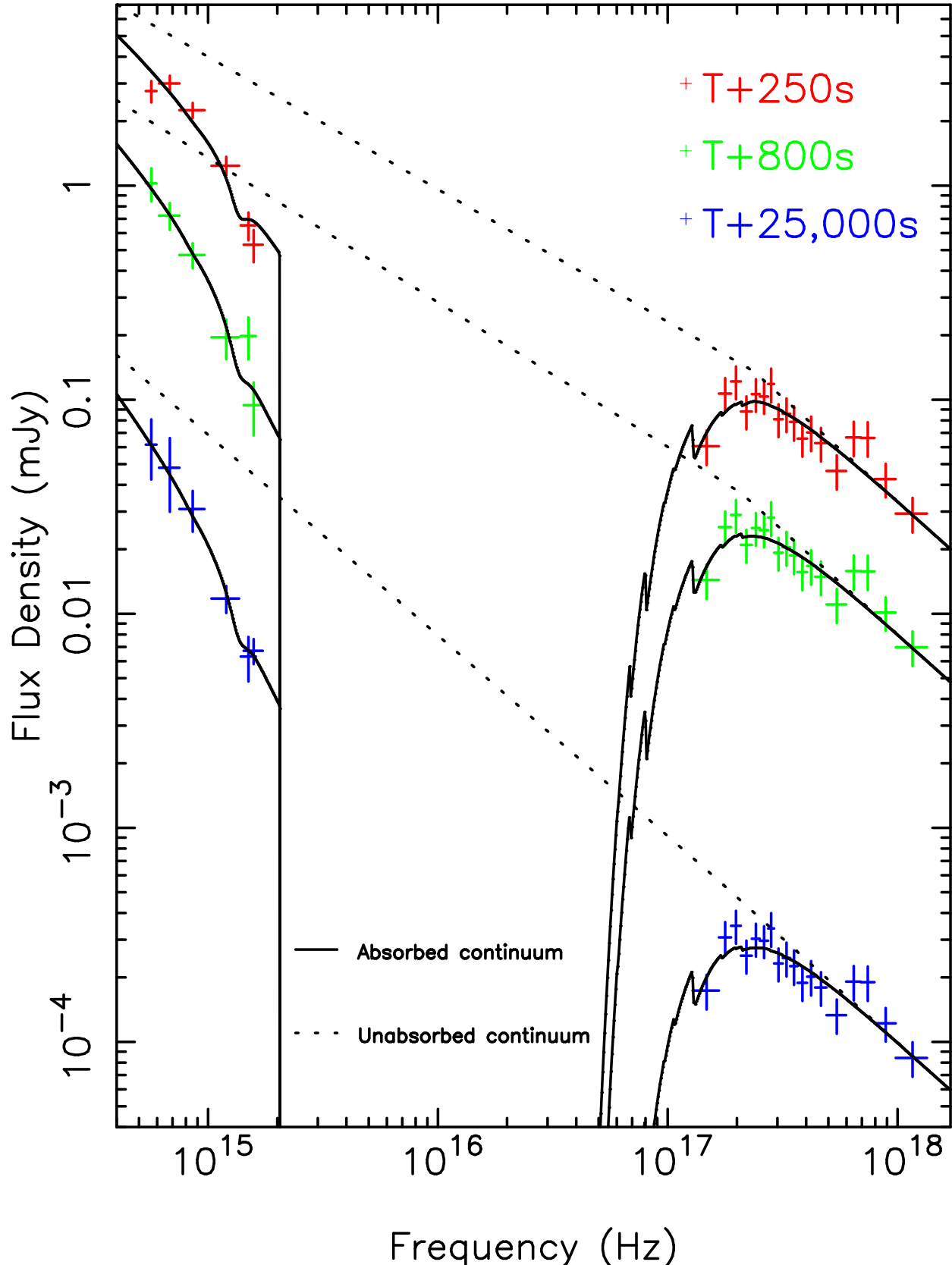


Fig. 8.— UVOT and XRT data interpolated to the epochs T+250s, T+800s and T+25,000s, and best spectral fit models (solid lines). The dotted lines represent the intrinsic continuum of the source, before extinction and absorption from gas and dust in both the Milky Way

telemetry rate. Event mode, and larger spatial windows, are emphasised at the beginning of the observing sequence, when the afterglow brightness is changing rapidly and its position is less well known. Later in the sequence only image mode data are taken. The intrinsic spatial pixel size of the detector is approximately 0.5 arc seconds on the sky, but some image mode data were taken with the data binned 2x2 to give 1 arc second pixels.

Examination of the UVOT finding chart exposure reveals a bright new fading source within the XRT positional error circle of the burst at RA = 18h 32m 32.62s Dec = +26d 20' 21.6" (J2000) with an estimated uncertainty of 0.2". This close to the ROTSE position given by Rykoff et al. (2005).

In Figure 4 we show the light curves in each of the UVOT bands as a function of time. These data were derived from measurements made in a 6 arcsec aperture, with background determined from a nearby source-free region. Since the UVOT detector counts individual photons, it is subject to coincidence loss (pile-up), which is noticeable for count rates above 10 per second. We have applied the standard coincidence loss correction to the data, derived from ground calibrations. The data have also been corrected for Galactic extinction, adopting a value of $E(B-V)=0.095$ for this field (Schlegel, Finkbeiner & Davis 1998). We used the data of Schlegel et al. (1998) and Pei et al. (1992) to derive extinction values for each filter. Expressed as magnitudes these are 0.688 (UVW2), 0.926 (UVM2), 0.740 (UVW1), 0.518 (U), 0.412 (B) & 0.316 (V). The data are tabulated in Table 3, separated by filter. The detector count rates have been converted to magnitudes and fluxes based on in-orbit calibration data. Systematic uncertainties between the filters are estimated to be better than 0.15 magnitudes.

After the source had faded below the threshold of detectability through the UVOT color filters, we made observations in unfiltered (white) light. The white light data provided detections of the afterglow beyond 10^5 s. We place the white light data on the V magnitude and flux scale using a color dependant correction that is derived by relating the measured ratio of V to white counts of field stars and photometric standards to their apparent B-V color (i.e. B-V color not corrected for reddening). The white light data are contained in Table 4.

2.3.1. Temporal Analysis

We fit a single power law to the light curve for each UVOT broadband filter individually, initially using only the data at $t \leq 1000$ s after the BAT trigger where the sampling for each individual filter is relatively dense. Each filter can be reasonably fit to a common slope of

$\alpha = -1.14 \pm 0.01$. We conclude that there is no evidence for a gross change in the optical/UV spectrum associated with the temporal decay.

To maximise the light curve sampling, we combine the data from all the UVOT filters, multiplying the individual curves by a factor that normalises them to a common flux scale. The results are shown in Figure 5. We also include for comparison the X-ray decay curve of Figure 4, which has been multiplied by a constant factor in Figure 5 for display purposes. It can be seen that the X-ray and optical/UV signals initially fade at a similar rate, but that the optical/UV flux flattens compared to the X-ray curve in the interval 1000-10000s (i.e. the ratio of optical to X-ray flux increases with time). After about 10000s the optical curve steepens in a similar way to the X-ray curve.

The complex nature of the optical/UV light curve is confirmed by the fact that a single power law does not provide a good fit to the combined UVOT data over the entire time range. The chi-square for the fit is 1038 for 115 degrees of freedom. We instead tried various combinations of power-laws and found that the best fit was obtained when we fit three power law components simultaneously. The model consists of the sum of two power laws (Holland et al. 2004) that breaks to a third, single power law at late time. This is physically consistent with the flux being dominated by a reverse shock at very early time, a forward shock at intermediate time, and a jet break at late time. The best fitting model had an early-time power law decay of $\alpha_1 = -1.56^{+0.07}_{-0.08}$ transitioning to a power law with a slope of $\alpha_2 = -0.62^{+0.05}_{-0.04}$ at $t_t = 432^{+173}_{-86}$ s. This transition time is the time at which both power law components contribute equally to the observed flux from the afterglow. An achromatic break occurs at $t_j = 13\,133^{+691}_{-691}$ s after the BAT trigger. We interpret this as a jet break. The decay slope after the jet break is $\alpha_j = -1.76^{+0.08}_{-0.08}$. The time of the jet break, and the post-break slope, are consistent with the values from the X-ray data. The chi-square value for this model is 555 for 111 degrees of freedom with most of the discrepancy arising from the two unusually bright V -band points at 18 676 s and 35 638 s. This model is compared to the individual filter data in Figure 6.

Klotz et al. (2005) find that the R -band light curve of the GRB 050525A afterglow underwent a sudden rebrightening of 0.65 mag at 1968 s after the BAT trigger. This was at a time when GRB050525a was not visible to Swift. We show the Klotz et al. data in Figure 7, normalised to the UVOT curve. If we add this rebrightening to our model the best fit has $\alpha_1 = -2.14^{+0.25}_{-0.26}$, $\alpha_2 = -1.04^{+0.02}_{-0.02}$, $\alpha_j = -1.73^{+0.08}_{-0.11}$, $t_t = 39^{+6}_{-6}$ s, and $t_j = 17\,747^{+1523}_{-1172}$ s with a chi-square of 597 for 111 degrees of freedom. Although the chi-square value is formally larger with a rebrightening, an examination of Figures 6 & 7 suggests that both models provide comparable fits.

2.3.2. Multiwavelength Spectral Analysis

Combining data across the Swift instruments provides a powerful set of diagnostics for prescribing the instantaneous spectral properties of a source and its temporal evolution. In order to fit an instantaneous spectral model to the UVOT data, it is necessary to interpolate count rates through each filter to a common epoch. We build a broad-band spectrum of the source at T+250s using the appropriate decay index for each filter, and the nearest exposure to T+250s as a normalization reference. The XRT spectrum described in section 2.2.2 was also renormalized to T+250s according to the early decay slope from Figure 3. As prior assumptions within the spectral model we take the XRT slope and 2–10 keV flux determined in section 2.2.2, the Galactic Hydrogen column density in the direction of the source of $9 \times 10^{20} \text{ cm}^{-2}$ (Dickey & Lockman 1990) and the Galactic extinction in the same direction characterized by Pei (1992) with $E(B-V) = 0.095$ (Schlegel et al 1988) and $R_V = 3.1$. Applying this model directly to the combined UVOT and XRT spectrum at T+250s yields a poor fit with $\chi^2 = 5.3 \times 10^4$ for 24 dof. This particular model systematically over-predicts the optical and UV flux. We attempt to correct this by first adding dust extinction and gas absorption from the host galaxy at a fixed redshift of $z = 0.606$. The dust is initially assumed to have a content identical to the SMC with $R_V = 2.93$ (Pei 1992). This does not provide an acceptable fit, with $\chi^2 = 272$ for 22 dof, where $N_H(\text{host}) = (1.8 \pm 0.8) \times 10^{21} \text{ cm}^{-2}$ and $E(B-V)(\text{host}) = 0.43 \pm 0.03$. Adopting host dust characteristics identical to the Galaxy and LMC populations (Pei 1992) does not improve the fit significantly, yielding $\chi^2 = 208$ and 242, respectively for 22 dof. An acceptable fit is, however, obtained if we add a spectral break to the model at 1 keV. Details of the fits to the model with a spectral break are provided in Table 5. The table includes results obtained using SMC, LMC and Galaxy dust distributions. The SMC prescription is preferred statistically over the other two.

We then perform spectral fits using the broken powerlaw model with SMC-like dust in the host galaxy for two other epochs, T+800s and T+25000s. Data and best-fit models are plotted in Figure 8 while best-fit parameters are listed in Table 6. Other than temporal decay, we find no evidence for spectral evolution between 200s and 800s after the burst; the spectral break has not moved within errors. However at T+25,000s the spectrum no longer requires a break between the XRT and UVOT energy bands. The UVOT spectral index is identical to the XRT slope, within measurement uncertainties. There is no evidence for evolution in the host’s gas or dust environments over these epochs.

Table 5. SED at T+250s

		SMC	LMC	Galaxy
$N_{\text{H}}(\text{host})$	(cm^{-2})	$1.2 \pm 0.8 \times 10^{21}$	$1.2 \pm 0.8 \times 10^{21}$	$1.2 \pm 0.8 \times 10^{21}$
β_1		-0.60 ± 0.04	-0.63 ± 0.03	-0.62 ± 0.04
β_2^*		-0.97	-0.97	-0.97
E_{break}	(keV)	1.0 ± 0.2	1.0 ± 0.2	$1.0 + / - 0.2$
$E(\text{B-V})(\text{host})$		0.04 ± 0.02	0.06 ± 0.03	0.06 ± 0.04
$\chi^2(\text{dof})$		27(20)	31(20)	41(20)

*Fixed parameter

Note. — Best fit spectral parameters for the SED of GRB 050525a at T+250s for three dust populations assumed for the host galaxy. The model continuum is a broken powerlaw (β_1 where $E < E_{\text{break}}$ and β_2 where $E > E_{\text{break}}$). The slope in the X-ray band, $\beta_2 = 0.97$, and the 2–10 keV flux are fixed at the XRT determined values. Galactic values for gas absorption and dust extinction are used, while the gas and dust properties of the host galaxy ($N_{\text{H}}(\text{host})$ and $E(\text{B-V})(\text{host})$) are allowed to float.

Table 6. The SMC-dust model from Table 5 applied to the GRB 050525a SED at three epochs.

		T+250s	T+800s	T+25,000s
$N_{\text{H}}(\text{host})$	(cm^{-2})	$1.2 \pm 0.8 \times 10^{21}$	$1.5 \pm 0.9 \times 10^{21}$	$1.8 \pm 1.0 \times 10^{21}$
β_1		-0.60 ± 0.04	-0.67 ± 0.06	-0.94 ± 0.10
β_2^*		-0.97	-0.97	-0.97
E_{break}	(keV)	1.0 ± 0.2	0.9 ± 0.2	–
$E(\text{B-V})(\text{host})$		0.04 ± 0.02	0.09 ± 0.04	0.08 ± 0.05
$\chi^2(\text{dof})$		27(20)	18(20)	15(20)

*Fixed parameter

3. Discussion

GRB050525a is the second most fluent GRB to have been observed by Swift to date, and is the first bright low redshift burst to have been observed since all three Swift instruments have been operational. The hard X-ray/Gamma-ray temporal characteristics and spectrum of this bright burst have been well characterised by the BAT. Added to this, the XRT and UVOT instruments provide well sampled temporal multiwavelength decay light curves and spectra starting about 1 minute after the burst trigger and extending to several days after the burst, making this one of the best covered GRBs thus far. The ratio of the gamma-ray fluence to the X-ray flux is typical of the general population of long bursts observed in the pre-Swift era (cf. Roming et al. 2005).

In an initial period of about 4 hours after the burst, the decline of the X-ray afterglow flux of GRB050525a can be well represented by a simple power law with an index -1.2 , apart from a probable flare which occurs after about 300s. The optical temporal signature is more complex, however, and exhibits a significant flattening over that same period. It can be reproduced by the combination of two power laws (or two power laws combined with a re-brightening episode), one declining more rapidly than the X-ray flux, and the other more slowly. This can be interpreted as the combination of a steep reverse shock component, combined with the flatter optical apparition of the forward shock seen in X-rays. The X-ray and optical/UV multiwavelength spectral fits suggest that the cooling frequency of the electrons in the forward shock has moved through the optical band by 25000s after the burst. There is good evidence for a break in the time evolution of both the X-ray and optical/UV data at ~ 0.15 days after the trigger. Its achromatic nature gives us confidence that this is the so-called jet break, which occurs when the beaming angle of the decelerating relativistic flow approaches the colimation angle of the jet (Sari, Piran & Halpern 1999).

A comparison of the temporal and spectral indices in the UVOT band and the XRT band with theoretical models (e.g. Table 1 in Zhang & Mészáros 2004), suggests that the data are not consistent with a model that invokes a massive stellar wind. Instead the XRT and UVOT data before the presumed jet break at 0.15 d are in good agreement with the standard fireball model for a constant ISM density (e.g. Sari, Piran & Narayan 1998). According to this model, the spectral indices (β) above and below the synchrotron cooling frequency ν_c are $-p/2$ and $-(p-1)/2$, respectively; while the temporal indices (α) for a band which is above and below ν_c are $(3-3p)/4$ and $(2-3p)/4$, respectively. The XRT-UVOT broad-band spectral fit shows a spectral break between the X-ray and optical/UV bands at $T + 250$ s and $T + 800$ s, which is suggestive of the cooling break. Taking $p = 2.2$, one expects $\alpha_X = -1.15$, $\alpha_O = -0.9$, $\beta_X = -1.1$, and $\beta_O = -0.6$. All these are in general agreement with the data. At $T + 25,000$ s, the UVOT band and the XRT band are consistent with a

single power law spectrum with index $\beta \sim -0.95$. This suggests that the cooling frequency has crossed the UVOT band by this epoch. According to the standard afterglow model, ν_c evolves with time as $\propto t^{-1/2}$. The data, on the other hand, require a slightly faster evolution of E_{break} . Enhanced cooling is thus needed, possibly with an evolving ϵ_B , the ratio of the magnetic energy density to the internal energy. An evolving ϵ_B was also invoked to interpret data on GRB 050128 (Campana et al. 2005).

A temporal break is identified in the X-ray lightcurve at around 0.15 d. The UVOT data show a break around the same time. Since there is no apparent spectral change across the break, and since the break time is “achromatic”, this points to a jet break, corresponding to the time when the fireball Lorentz factor $\gamma \sim 1/\theta_j$ (Rhoads 1999; Sari, Piran & Halpern 1999). The post-break temporal index, however, is shallow (~ -1.6) compared with the model prediction (which is $\sim -p = -2.2$). This might be because the sideways expansion effect is not significant. Alternatively, the jet break turn-over time may be finite (Panaitescu & Mészáros 1999), so that the post-break asymptotic temporal regime has not yet been reached. The late X-ray afterglow data are consistent with a steeper decay which suggests a possible roll-over for the jet break.

If the break is indeed attributed to a jet, one can derive a jet angle (e.g. Sari et al. 1999)

$$\theta_j = 0.12 \left(\frac{t_j}{1+z} \right)^{3/8} \left(\frac{n_0 \eta_\gamma}{E_{iso,53}} \right)^{1/8} = 4.6 \times 10^{-2} (10 n_0 \eta_\gamma)^{1/8}, \quad (1)$$

where t_j is expressed in days. This angle, which corresponds to $\sim 2.5^\circ$, could be interpreted as the physical opening angle of jet if the jet has a uniform distribution of energy, or as the observer’s viewing angle with respect to the jet axis in a structured jet model (Rossi et al. 2002; Zhang & Mészáros 2002; Kumar & Granot 2003). Within the uniform jet model, we estimate the actual gamma-ray energy emitted to be $E_\gamma = E_{iso,\gamma} (1 - \cos \theta_j) = 4.9 \times 10^{49}$ ergs, assuming the ambient density $n_0 = 1 \text{ cm}^{-3}$ and the ejecta-to-gamma-ray efficiency $\eta_\gamma = 0.1$.

We can combine the information on the jet with the measures of the redshift, E_p , $E_{iso,\gamma}$ and the lag between the high energy and low energy Gamma ray light curves (section 2.1) to test whether this burst is consistent with various proposed empirical relations. Three relations involve E_{pt} , the peak energy in the burst frame for the entire burst: the Amati relation— $E_{pt,Amati} \propto E_{iso}^{0.5}$ (Amati et al. 2002); the Ghirlanda relation— $E_{pt,Ghirlanda} \propto E_\gamma^{0.7}$ (Ghirlanda, Ghisellini & Lazzati 2004); and the Yonetoku relation— $E_{pt,Yonetoku} \propto L_{iso}^{0.5}$ (Yonetoku et al. 2004). For GRB 050525a’s values of E_{iso} , E_γ and L_{iso} , we calculate $E_{pt,Amati}=144 \text{ keV}$, $E_{pt,Ghirlanda}=58 \text{ keV}$, and $E_{pt,Yonetoku}=186 \text{ keV}$, which should be compared to the observed value of $E_{pt} = 126.6 \pm 5.5 \text{ keV}$. The set of bursts used to calibrate these relations shows significant scatter around the relations, and therefore we consider

GRB 0505025a to be discrepant only with the Ghirlanda relation.

According to the lag-luminosity relation, shorter lags between the emission in two gamma-ray bands are correlated with larger L_{iso} (Norris, Marani & Bonnell 2000). Using the methodology in Band, Norris & Bonnell (2004), we calculate a redshift $\hat{z} = 0.69 \pm 0.02$ for GRB050525a from the observed values of the peak flux, lag and spectrum at the peak of the lightcurve (Norris et al. 2005); the uncertainty in this derived time-lag redshift accounts for the uncertainty in the lag and the peak flux, but not for the systematic uncertainty resulting from the somewhat different energy bands used to calibrate the lag-luminosity relation and for the *Swift* observation. Given the large redshift range over which bursts are detected, the agreement between this time-lag redshift and the spectroscopic redshift is impressive.

The UVOT lightcurves are consistent with the existence of an early reverse shock component (Mészáros & Rees 1997; Sari & Piran 1999). The best-fit initial decay index is sensitive to whether we include a re-brightening episode in our model, as suggested by Klotz et al. (2005). It ranges from $\alpha_1 \sim -1.5$ without re-brightening to $\alpha_1 \sim -2.1$ with re-brightening. This is in the range observed for previous suggested detections of the reverse shock in GRB 990123 (Akerlof 1999) and GRB 021211 (Fox et al. 2003; Li et al. 2003), which are typically ~ -1.9 . A shallower decay corresponds to a shallower electron index in the reverse shock region, $p = (-4\alpha_1 - 1)/3 \sim 1.75$ (Zhang, Kobayashi & Mészáros 2003). In contrast with Shao & Dai (2005) who interpreted the tentative jet break as the forward shock peak, in our best fit, the forward shock peaks at a much earlier time, before 400 s. This corresponds to a typical “flattening”-type early afterglow (Zhang et al. 2003), which usually requires a magnetized central engine (see also Fan et al. 2002; Kumar & Panaitescu 2003). The best fit temporal index that we derive for the forward shock component in the optical/UV without a re-brightening is -0.62, flatter than the expectation of the simplest model (-0.9). However if we include a re-brightening episode as described above, the slope of the forward shock component steepens to -1.04, which would be more consistent with the simple model.

The Swift programme is supported by NASA, PPARC and ASI (contract number I/R/039/04).

REFERENCES

Akerlof, C., et al., 1999, *Nature*, 398, 400.

Amati, L., et al. 2002, *A&A*, 390, 81.

Band, D. L., Norris, J. P. & Bonnell, J. T. 2004, *ApJ*, 613, 484.

Band, D., et al. 1993, *ApJ*, 413, 281.

Band, D. et al. 2005 GCN Circ 3466.

Barthelmy, S. et al. 2005 *Space Sci Rev* (in press).

Burrows, D. et al. 2005a *Space Sci Rev* (in press).

Burrows, D. et al. 2005b *Science* (in press).

Campana, S. et al. 2005, *ApJ*, 625, L23.

Chincarini, G. et al. 2005, *ApJ*, (submitted; astro-ph/0506453).

Costa, E., et al., 1997, *Nature*, 387, 783.

Cummings, J. et al. 2005 GCN Circ 3479.

Fan, Y. Z., Dai, Z. G., Huang, Y. F. & Lu, T. 2002, *ChJAA*, 2, 449.

Foley, R. J., Chen, H.-W., Bloom, J. & Prochaska, J. X. 2005, GCN Circ 3483.

Fox, D. et al. 2003, *ApJ*, 586, L5.

Frail, D. A., Kulkarni, S. R., Nicastro, S. R., Feroci, M., & Taylor, G. B., 1997, *Nature*, 389, 261.

Gehrels, N. et al. 2004 *Ap.J.* 611, 1005.

Ghirlanda, G., Ghisellini, G., & Lazzati, D. 2004, *ApJ*, 616, 331.

Golenetskii, S., Aptekar, R., Mazets, E., Pal'shin, Z., Frederiks, D. & Cline, T. 2005, GCN Circular 3474.

Gotz, D., Mereghetti, S., Mowlavi, N., Shaw, S., Beck, M., Borkowski, J., & Lund, N. 2005, GCN Circular 3472.

Heise, J., et al., 1997, *IAU Circular*, 6654.

Holland, S. T., et al. 2004, *Astron. J.*, 128, 1955.

Klebesadel, R. W., Strong, I. B., & Olson, R. A., 1973, *ApJ*, 182, L85.

Klotz, A., Boér, M., Atteia, J. L., Stratta, G., Behrend, R., Malacrino, F., & Darmedji, Y. 2005, *Astron. Astrophys.*, submitted, astro-ph/0506259

Kouveliotou, C., Meegan, C. A., Fishman, G. J., Bhat, N. P., Briggs, M. S., Koshut, T. M., Paciesas, W. S., & Pendleton, G. N., 1993, *ApJ*, 413, L101.

Kulkarni, S. R., et al., 1999, *ApJ*, 522, L97.

Kumar, P. & Granot, J. 2003, *ApJ*, 591, 1075.

Kumar, P. & Panaiteescu, A. 2003, *MNRAS*, 346, 905.

Li, W. et al. 2003, *ApJ*, 586, L9.

Meegan, C. A., Fishman, G. J., Wilson, R. B., Horack, J. M., Brock, M. N., Paciesas, W. S., Pendleton, G. N., & Kouveliotou, C., 1992, *Nature*, 355, 143.

Mereghetti, S., et al. 2005, GCN3477.

Metzger, M. R., et al., 1997, *Nature*, 387, 878.

Mészáros, P. & Rees, M. J. 1997, *ApJ*, 476, 232.

Norris, J., et al. 2005, *GCN Circular* 3484.

Norris, J. P., Marani, G. F., & Bonnell, J. T. 2000, *ApJ*, 534, 248.

Panaiteescu, A. & Mészáros, P. 1999, *ApJ*, 526, 707

Piro, L. et al. 2005, *ApJ*, 623, 314.

Rhoads, J. E. 1999, *ApJ*, 525, 737

Roming, P. et al. 2005 *Space Sci Rev* (in press).

Roming, P. et al. 2005 *Ap.J.Lett.* (in press).

Rossi, E., Lazzati, D. & Rees, M. J. 2002, *MNRAS*, 332, 945

Rykoff, E. S., Yost, S. A., Swan, H., & Quimby, R. 2005, GCN3468.

Sari, R. & Piran, T. 1999, *ApJ*, 517, L109

Sari, R., Piran, T. & Narayan, R. 1998, *ApJ*, 497, L17.

Sari, R., Piran, T. & Halpern, J. P. 1999, *ApJ*, 519, L17.

Schlegel, D. J., Finkbeiner, D. P. & Davis, M. 1998, *ApJ*, 500, 525.

Shao, L. & Dai, Z. G. 2005, preprint, astro-ph/0506139.

Soderberg, A. 2005, GCN Circular 3550.

Yonetoku, D., Murakami, T., Nakamura, T., Yamazaki, R., Inoue, A. K., & Ioka, K. 2004, *ApJ*, 609, 935.

Zhang, B., Kobayashi, S. & Mészáros, P. 2003, *ApJ*, 595, 950

Zhang, B. & Mészáros, P. 2002, *ApJ*, 571, 876

Zhang, B. & Mészáros, P. 2004, *IJMPC*, 19, 2385